ORIGINAL PAPER

Computational and experimental investigation of free vibration and flutter of bridge decks

Tore A. Helgedagsrud[1] · Yuri Bazilevs[2] · Kjell M. Mathisen[1] · Ole A. Øiseth[1]

Abstract

A modified rigid-object formulation is developed, and employed as part of the fluid–object interaction modeling framework from Akkerman et al. (J Appl Mech 79(1):010905, 2012. https://doi.org/10.1115/1.4005072) to simulate free vibration and flutter of long-span bridges subjected to strong winds. To validate the numerical methodology, companion wind tunnel experiments have been conducted. The results show that the computational framework captures very precisely the aeroelastic behavior in terms of aerodynamic stiffness, damping and flutter characteristics. Considering its relative simplicity and accuracy, we conclude from our study that the proposed free-vibration simulation technique is a valuable tool in engineering design of long-span bridges.

Keywords Flutter · Numerical methods · Solid–fluid interaction · Rigid bodies · Wind

1 Introduction

The Finite Element Method (FEM) has in recent decades seen significant development in accurate modeling in Computational Fluid Dynamics (CFD) and Fluid–Structure Interaction (FSI), which are, with the increasing computer power, gaining a growing foothold in engineering design [2]. An FSI problem becomes a Fluid–Object Interaction (FOI) problem when deformations of the structure can be neglected. The solid part of the problem is then approximated by a rigid object, and the equation system for the structural part reduces to the balance of global linear and angular momenta with respect to the center of mass, yielding a system of only three equations in 2D and six equations in 3D. Earlier coupling between CFD and rigid objects was reported in [3] for a cylinder drifting in shear flow and in [4] for vortex-induced vibrations of a cylinder. Other earlier FOI work was reported in conjunction with the Mixed Interface-Tracking/Interface-Capturing Technique (MITICT) in e.g., [5,6]. Recently FOI

methods have been employed in several marine applications in the study of free-surface flows [1,7–9]. In the context of bridge engineering, FOI has been used to study the effect of railings and spoilers on the Hardanger bridge [2] and to simulate the flutter phenomenon for the Great Belt East suspension bridge [10,11]. However, any direct time-domain validation of free-vibration wind-tunnel experiments are, to the authors' knowledge, not reported in open literature.

In the present work, the aerodynamics part of the FOI problem is solved using the Arbitrary Lagrangian–Eulerian Variational Multiscale (ALE-VMS) formulation of the Navier–Stokes equations for incompressible flows [2,12–16] augmented with the weakly-enforced boundary conditions [17–19]. This method, which is a moving-mesh method, has proven very effective in a wide range of turbulent flow problems, see e.g., [20–23], including bridge aerodynamics [24–26]. In the category of moving-mesh methods, the Space-Time VMS (ST-VMS) method [27,28] has also proven effective in a wide range of problems, including flapping wings [29,30], heart valve flow [31,32], disk brake thermo-fluids [33], turbomachinery [34–36], and tire aerodynamics with road contact and tire deformation [37].

In engineering design of long-span bridges, aerodynamic performance and stability is one of the major concerns. The aerodynamic stability, which is governed by the self-excited forces, is traditionally studied on small-scale models in the wind tunnel, however, numerous studies [2,10,11,24,38–43]

✉ Tore A. Helgedagsrud
tore.a.helgedagsrud@ntnu.no

[1] Department of Structural Engineering, NTNU - Norwegian University of Science and Technology, Richard Birkelands v 1a, 7491 Trondheim, Norway

[2] School of Engineering, Brown University, 184 Hope Street, Providence, RI 02912, USA

prove CFD and FSI to be a valuable supplement. Most of these studies used the forced-vibration method with a prescribed bridge-deck motion, due to its repeatability, effectiveness and simple identification procedures. For the same reasons, this is also the preferred method in wind-tunnel experiments [44,45]. However, the free-vibration method, in which the bridge deck is suspended by springs and allowed to vibrate freely, has the advantage of exhibiting the response to wind action directly, rather than filtered through a semi-empirical load theory applied in the forced-vibration method [46]. Therefore, this method is commonly used to validate the forced-vibration results. Another benefit of using the free-vibration technique is that the general aerodynamic performance can be determined directly, rather than from a model that relies on the parameters obtained with the forced-vibration approach.

In this work we use a coupled analysis of the ALE-VMS formulation with weakly-enforced boundary conditions and a modified rigid-object formulation to simulate free-vibration wind tunnel tests of bridge sections. We take the rigid-body dynamics formulation from [1] and augment it with external stiffness and damping to represent the effect of the suspension. Further, we propose a simplified time-integration algorithm that assumes a linear relationship between the time derivative of the Euler angles and rotation vector in the linearization of the rigid-object angular-momentum equations. The formulation is tested on a 1:50 scale model of the Hardanger bridge section at various wind speeds. Several studies have been performed on the same section experimentally [45,47] and numerically by the same authors using the forced-vibration method [25,26].

To validate the numerical simulations we have also conducted free-vibration wind tunnel experiments of the same bridge section. The focus in this work has been to evaluate how the formulation is capable of capturing the aerodynamic contribution to the dynamic properties of the coupled system. The aerodynamic damping, which is the driving mechanism of flutter instability, is of particular interest. We consider four wind speeds, including still-wind and the critical wind speed at which flutter occurs.

The paper is organized as follows. The governing equations are presented in the continuous form in Sect. 2 and in the discrete form in Sect. 3. Section 4 introduces the aerodynamic forces with emphasis on flutter analysis. The setup for wind-tunnel experiments and numerical simulations is presented in Sect. 5. The numerical results are presented in Sect. 6 before conclusions are drawn in Sect. 7.

2 Governing equations

In this section we present the governing equations for the aerodynamics rigid-object problems.

2.1 Aerodynamics

The Navier–Stokes equations of incompressible flows in an ALE frame [48] govern the aerodynamics of the problem and are stated as follows. Let $\hat{\Omega} \in \mathbb{R}^{n_{sd}}$, $n_{sd} = 2, 3$, represent the reference fluid mechanics domain with coordinates $\hat{\mathbf{x}}$ and boundary $\hat{\Gamma}$, and let $\Omega_t \in \mathbb{R}^{n_{sd}}$, $n_{sd} = 2, 3$, represent the time dependent fluid mechanics domain in the current configuration with coordinates $\mathbf{x}$ and boundary Γ_t. With these definitions, the continuous linear-momentum and mass-balance equations on Ω_t are given, respectively, as

$$\rho \left(\left. \frac{\partial \mathbf{u}}{\partial t} \right|_{\hat{x}} + (\mathbf{u} - \hat{\mathbf{u}}) \cdot \nabla \mathbf{u} - \mathbf{f} \right) - \nabla \cdot \boldsymbol{\sigma} = 0, \tag{1}$$

$$\nabla \cdot \mathbf{u} = 0, \tag{2}$$

where $\boldsymbol{\sigma}$ is the Cauchy stress tensor defined as

$$\boldsymbol{\sigma} (\mathbf{u}, p) = -p\mathbf{I} + 2\mu \, \boldsymbol{\varepsilon}(\mathbf{u}). \tag{3}$$

In the above, $\mathbf{u}$, p and ρ are the fluid velocity, pressure and density, respectively. μ is the dynamic viscosity and $\boldsymbol{\varepsilon}(\mathbf{u})$ is the symmetric gradient of $\mathbf{u}$. In addition, $\hat{\mathbf{u}}$ is the velocity of the fluid domain and $\mathbf{f}$ is the body force per unit mass. The subscript $|_{\hat{x}}$ on the partial derivative in Eq. (1) denotes that the time derivative is taken with the referential coordinates $\hat{\mathbf{x}}$ fixed. The spatial derivatives in Eqs. (1)–(3) are taken with respect to $\mathbf{x}$.

2.2 Rigid object

Using the notation in Fig. 1, we let Ω_0^b denote the rigid-object reference configuration with coordinates $\mathbf{X}$ and center of mass $\mathbf{X}_0$, and we let Ω_t^b denote the rigid-object current configuration with coordinates $\mathbf{x}$ and center of mass $\mathbf{x}_0$. All rigid-object motions can be described by a translation and rotation of its center of mass as

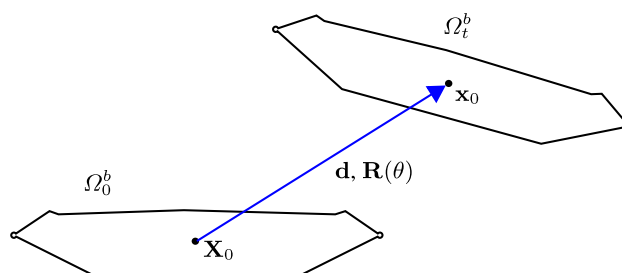$$\mathbf{x} = \mathbf{R} (\mathbf{X} - \mathbf{X}_0) + \mathbf{x}_0, \tag{4}$$

Fig. 1 Rigid body, represented by a bridge cross section, in its reference and current configuration

where $\mathbf{R}$ is the rotation tensor. From Eq. (4) we obtain the displacement field as

$$\mathbf{y} = \mathbf{x} - \mathbf{X} = (\mathbf{R} - \mathbf{I})(\mathbf{X} - \mathbf{X}_0) + \mathbf{d}, \tag{5}$$

where $\mathbf{d}$ is the displacement of the center of mass.

We take the material time derivative in Eq. (5) to obtain the velocity field

$$\mathbf{u} = \dot{\mathbf{R}}(\mathbf{X} - \mathbf{X}_0) + \mathbf{v}, \tag{6}$$

where $\mathbf{v}$ is the velocity of the center of mass. Using Eq. (4), we can express the velocity field in Eq. (6) in terms of the current coordinates as

$$\mathbf{u} = \boldsymbol{\Omega}(\mathbf{x} - \mathbf{x}_0) + \mathbf{v}, \tag{7}$$

where $\boldsymbol{\Omega}$ is the skew-symmetric tensor of angular velocities:

$$\boldsymbol{\Omega} = \dot{\mathbf{R}}\mathbf{R}^{-1} = \begin{bmatrix} 0 & -\omega_3 & \omega_2 \\ \omega_3 & 0 & -\omega_1 \\ -\omega_2 & \omega_1 & 0 \end{bmatrix}. \tag{8}$$

Further, we define $\boldsymbol{\omega}$, the axial vector of $\boldsymbol{\Omega}$, as

$$\boldsymbol{\omega} = \begin{bmatrix} \omega_1 \\ \omega_2 \\ \omega_3 \end{bmatrix}. \tag{9}$$

Eq. (7) can then be written as

$$\mathbf{u} = \boldsymbol{\omega} \times (\mathbf{x} - \mathbf{x}_0) + \mathbf{v}. \tag{10}$$

Note that from Eq. (8) it follows that

$$\dot{\mathbf{R}} = \boldsymbol{\Omega}\mathbf{R}, \tag{11}$$

which is used as the generating equation for $\mathbf{R}$.

The rigid-object motion is governed by the balance of global linear and angular momenta, expressed, respectively, as

$$\frac{\mathrm{d}}{\mathrm{d}t}(m\mathbf{v}) + \mathbf{C}^{lin}\mathbf{v} + \mathbf{K}^{lin}\mathbf{d} = \mathbf{F}, \tag{12}$$

and

$$\frac{\mathrm{d}}{\mathrm{d}t}(\mathbf{J}_t\boldsymbol{\omega}) + \mathbf{C}^{ang}\boldsymbol{\omega} + \mathbf{K}^{ang}\boldsymbol{\theta} = \mathbf{M}. \tag{13}$$

In the above equations, $\mathbf{v}$ and $\mathbf{d}$ are the center-of-mass velocity and displacement, respectively, $\boldsymbol{\omega}$ and $\boldsymbol{\theta}$ are the axial vectors of angular velocities and Euler angles, respectively, and

m and $\mathbf{J}_t$ are the object mass and current-configuration inertia tensor, respectively. The latter quantity may be expressed as

$$\mathbf{J}_t = \mathbf{R}\mathbf{J}_0\mathbf{R}^T, \tag{14}$$

where the reference-configuration inertia tensor, $\mathbf{J}_0$, is given by

$$\mathbf{J}_0 = \int_{\Omega_0^b} \rho(\mathbf{X} - \mathbf{X}_0) \cdot (\mathbf{X} - \mathbf{X}_0)\mathbf{I}\mathrm{d}\Omega$$
$$- \int_{\Omega_0^b} \rho(\mathbf{X} - \mathbf{X}_0) \otimes (\mathbf{X} - \mathbf{X}_0)\,\mathrm{d}\Omega. \tag{15}$$

In Eq. (12), $\mathbf{C}^{lin}$ and $\mathbf{K}^{lin}$ are the linear damping and stiffness matrices, while in Eq. (13) $\mathbf{C}^{ang}$ and $\mathbf{K}^{ang}$ are their torsional counterparts. We note that the vector of Euler angles $\boldsymbol{\theta}$ may be obtained from the rotation matrix $\mathbf{R}$.

Finally, vectors $\mathbf{F}$ and $\mathbf{M}$ represent the external forces and moments acting on the rigid object and are given by

$$\mathbf{F} = m\mathbf{g} + \int_{\Gamma_t^I} \mathbf{h}\,\mathrm{d}\Gamma, \tag{16}$$

and

$$\mathbf{M} = \int_{\Gamma_t^I} (\mathbf{x} - \mathbf{x}_0) \times \mathbf{h}\,\mathrm{d}\Gamma, \tag{17}$$

where $\mathbf{g}$ is the gravitational acceleration vector, and $\mathbf{h}$ is the aerodynamic traction vector acting on the object surface Γ_t^I. Note that gravity does not contribute to Eq. (17) because it creates zero moment around the center of mass.

3 Discrete formulation

The discrete formulation of the coupled FOI problem is presented in what follows. We emphasize the rigid-object formulation, and for a more thorough description of the aerodynamics and mesh motion parts of the problem the reader is referred to [20] and references therein.

3.1 ALE-VMS formulation

At the discrete level, the fluid domain is partitioned into n_{el} finite element subdomains Ω_t^e and its boundary into n_{eb} surface elements Γ_t^b. We then define finite-dimensional trial functions for the fluid velocity $\mathbf{u}$ and pressure p, denoted $\mathcal{S}_u^h$ and $\mathcal{S}_p^h$, respectively, and their corresponding test functions $\mathcal{V}_u^h$ and $\mathcal{V}_p^h$. Superscript h indicate that its attribute is finite-dimensional.

The semi-discrete ALE-VMS formulation is then given as follows. Find $\mathbf{u}^h \in \mathcal{S}_u^h$ and $p^h \in \mathcal{S}_p^h$, such that $\forall \mathbf{w}^h \in \mathcal{V}_u^h$ and $q^h \in \mathcal{V}_p^h$:

$$
\begin{aligned}
&\int_{\Omega_t} \mathbf{w}^h \cdot \rho \left(\left. \frac{\partial \mathbf{u}^h}{\partial t} \right|_{\hat{x}} + \left(\mathbf{u}^h - \hat{\mathbf{u}}^h \right) \cdot \nabla \mathbf{u}^h \right) d\Omega \\
&+ \int_{\Omega_t} \boldsymbol{\varepsilon}(\mathbf{w}^h) : \boldsymbol{\sigma}(\mathbf{u}^h, p^h) \, d\Omega + \int_{\Omega_t} q^h \nabla \cdot \mathbf{u}^h \, d\Omega \\
&- \int_{\Omega_t} \mathbf{w}^h \cdot \rho \, \mathbf{f}^h \, d\Omega - \int_{(\Gamma_t)_h} \mathbf{w}^h \cdot \mathbf{h}^h \, d\Gamma \\
&+ \sum_{e=1}^{n_{el}} \int_{\Omega_t^e} \tau_{\text{SUPS}} \left(\left(\mathbf{u}^h - \hat{\mathbf{u}}^h \right) \cdot \nabla \mathbf{w}^h + \frac{\nabla q^h}{\rho} \right) \\
&\cdot \mathbf{r}_M \left(\mathbf{u}^h, p^h \right) d\Omega \\
&+ \sum_{e=1}^{n_{el}} \int_{\Omega_t^e} \rho \nu_{\text{LSIC}} \nabla \cdot \mathbf{w}^h \mathrm{r}_C(\mathbf{u}^h) \, d\Omega \\
&- \sum_{e=1}^{n_{el}} \int_{\Omega_t^e} \tau_{\text{SUPS}} \mathbf{w}^h \cdot \left(\mathbf{r}_M \left(\mathbf{u}^h, p^h \right) \cdot \nabla \mathbf{u}^h \right) d\Omega \\
&- \sum_{e=1}^{n_{el}} \int_{\Omega_t^e} \frac{\nabla \mathbf{w}^h}{\rho} : \left(\tau_{\text{SUPS}} \mathbf{r}_M \left(\mathbf{u}^h, p^h \right) \right) \\
&\otimes \left(\tau_{\text{SUPS}} \mathbf{r}_M \left(\mathbf{u}^h, p^h \right) \right) d\Omega = 0
\end{aligned}
\tag{18}
$$

In Eq. (18) $\mathbf{r}_M$ and r_C are residuals of the Navier–Stokes linear-momentum balance and continuity, respectively, given as

$$
\mathbf{r}_M = \rho \left(\left. \frac{\partial \mathbf{u}^h}{\partial t} \right|_{\hat{x}} + \left(\mathbf{u}^h - \hat{\mathbf{u}}^h \right) \cdot \nabla \mathbf{u}^h - \mathbf{f}^h \right) - \nabla \cdot \boldsymbol{\sigma} \left(\mathbf{u}^h, p^h \right),
\tag{19}
$$

$$
\mathrm{r}_C = \nabla \cdot \mathbf{u}^h.
\tag{20}
$$

τ_{SUPS} and ν_{LSIC} are stabilization parameters which are designed to render optimal stability and convergence through extensive studies, see e.g., [49–58] and references therein, and are adopted from the definitions given in [59].

The surface tractions $\mathbf{h}^h$ are evaluated on the $(\Gamma_t)_h$ part of Γ_t. The essential boundary conditions are specified on the $(\Gamma_t)_g$ part of Γ_t, and are imposed weakly by adding the following terms to the left-hand side of Eq. (18):

$$
\begin{aligned}
&- \sum_{b=1}^{n_{eb}} \int_{\Gamma_t^b \cap (\Gamma_t)_g} \mathbf{w}^h \cdot \boldsymbol{\sigma} \left(\mathbf{u}^h, p^h \right) \mathbf{n} \, d\Gamma \\
&- \sum_{b=1}^{n_{eb}} \int_{\Gamma_t^b \cap (\Gamma_t)_g} \left(2\mu \boldsymbol{\varepsilon} \left(\mathbf{w}^h \right) \mathbf{n} + q^h \mathbf{n} \right) \cdot \left(\mathbf{u}^h - \mathbf{g}^h \right) d\Gamma \\
&- \sum_{b=1}^{n_{eb}} \int_{\Gamma_t^b \cap (\Gamma_t)_g^-} \mathbf{w}^h \cdot \rho \left(\left(\mathbf{u}^h - \hat{\mathbf{u}}^h \right) \cdot \mathbf{n} \right) \left(\mathbf{u}^h - \mathbf{g}^h \right) d\Gamma
\end{aligned}
$$

$$
\begin{aligned}
&+ \sum_{b=1}^{n_{eb}} \int_{\Gamma_t^b \cap (\Gamma_t)_g} \tau_{\text{TAN}} \left(\mathbf{w}^h - \left(\mathbf{w}^h \cdot \mathbf{n} \right) \mathbf{n} \right) \\
&\cdot \left(\left(\mathbf{u}^h - \mathbf{g}^h \right) \left(\left(\mathbf{u}^h - \mathbf{g}^h \right) \cdot \mathbf{n} \right) \mathbf{n} \right) d\Gamma \\
&+ \sum_{b=1}^{n_{eb}} \int_{\Gamma_t^b \cap (\Gamma_t)_g} \tau_{\text{NOR}} \left(\mathbf{w}^h \cdot \mathbf{n} \right) \left(\left(\mathbf{u}^h - \mathbf{g}^h \right) \cdot \mathbf{n} \right) d\Gamma.
\end{aligned}
\tag{21}
$$

Here $\mathbf{n}$ is the unit outward normal vector, τ_{TAN} and τ_{NOR} are the boundary penalty parameters in the tangential and normal directions, respectively, as defined in [17], and $(\Gamma_t)_g^-$ is defined as the inflow part of $(\Gamma_t)_g$:

$$
(\Gamma_t)_g^- = \left\{ \mathbf{x} | \left(\mathbf{u}^h - \hat{\mathbf{u}}^h \right) \cdot \mathbf{n} < 0, \forall \mathbf{x} \subset (\Gamma_t)_g \right\}.
\tag{22}
$$

3.2 Mesh-moving technique

We make use of an interface-tracking technique [60], where the computed displacement and velocity of the rigid object define the kinematics of the fluid-rigid-object interface and are prescribed as essential boundary conditions in the fluid mesh-moving problem.

We assign the variable $\hat{\mathbf{y}}(t)$ to the fluid domain displacement, such that $\frac{d\hat{\mathbf{y}}}{dt} = \hat{\mathbf{u}}$ at the fluid-rigid-object interface, and define its trial and test function respectively as $\mathcal{S}_y^h$ and $\mathcal{V}_y^h$. The displacements of the fluid domain interior can then be found by solving the linear elastostatics problem in the weak form: Find $\hat{\mathbf{y}}^h \in \mathcal{S}_y^h$ such that $\mathbf{w}_y^h \in \mathcal{V}_y^h$:

$$
\int_{\Omega_{\tilde{t}}} \boldsymbol{\varepsilon}(\mathbf{w}_m^h) : \mathbf{D}^h \, \boldsymbol{\varepsilon} \left(\hat{\mathbf{y}}^h(t) - \hat{\mathbf{y}}^h(\tilde{t}) \right) d\Omega = 0.
\tag{23}
$$

Here $\Omega_{\tilde{t}}$ and $\hat{\mathbf{y}}^h(\tilde{t})$ are the fluid mesh nearby configuration and displacement at time $\tilde{t} < t$, in practice taken at the previous time step. The elastic tensor $\mathbf{D}^h$ is defined in terms of mesh-dependent Lamé parameters μ^h and λ^h as given in [1]. With this definition the element Young's modulus is proportional with the inverse of the Jacobian, making smaller element stiffer and minimize the mesh distortion. This method, introduced in [61–63], was named Jacobian-based stiffening in [60].

3.3 Time integration of rigid-object equations

In what follows, we present the time integration algorithm of the rigid-object equations given in Sect. 2.2. Following [64], we employ the midpoint rule in order to preserve the orthonormal properties of the rotation tensor.

Starting with the balance of linear momentum in Eq. (12), the midpoint approximation reads

$$\frac{m\,(\mathbf{v}_{n+1} - \mathbf{v}_n)}{\Delta t} + \mathbf{C}^{lin}\frac{\mathbf{v}_{n+1} + \mathbf{v}_n}{2} + \mathbf{K}^{lin}\frac{\mathbf{d}_{n+1} + \mathbf{d}_n}{2} = \mathbf{F}_{n+1/2}. \quad (24)$$

We define the discrete residual vector of linear-momentum equation, $\mathbf{N}^{lin}$, as

$$\mathbf{N}^{lin}\,(\mathbf{v}_{n+1}) = \frac{m\,(\mathbf{v}_{n+1} - \mathbf{v}_n)}{\Delta t} + \mathbf{C}^{lin}\frac{\mathbf{v}_{n+1} + \mathbf{v}_n}{2} \\ + \mathbf{K}^{lin}\frac{\mathbf{d}_{n+1} + \mathbf{d}_n}{2} - \mathbf{F}_{n+1/2}. \quad (25)$$

The corresponding linearized equation system then reads

$$\frac{\partial \mathbf{N}^{lin}}{\partial \mathbf{v}_{n+1}}\Delta\mathbf{v}_{n+1} = -\mathbf{N}^{lin}\,(\mathbf{v}_{n+1})\,, \quad (26)$$

where the left-hand side matrix becomes

$$\frac{\partial \mathbf{N}^{lin}}{\partial \mathbf{v}_{n+1}} = \frac{m}{\Delta t}\mathbf{I} + \frac{1}{2}\mathbf{C}^{lin} + \frac{\Delta t}{4}\mathbf{K}^{lin}. \quad (27)$$

In the above equation we used the fact that relationship between $\mathbf{d}$ and $\mathbf{v}$ is also approximated using a midpoint rule, which gives

$$\frac{\partial \mathbf{d}_{n+1}}{\partial \mathbf{v}_{n+1}} = \frac{\Delta t}{2}\mathbf{I}, \quad (28)$$

and thus explains the factor $\frac{\Delta t}{4}$ in front of the $\mathbf{K}^{lin}$ term in Eq. (27).

We likewise form a discrete residual vector from the angular-momentum Eq. (13) integrated using a midpoint rule:

$$\mathbf{N}^{ang}(\boldsymbol{\omega}_{n+1}) = \frac{\mathbf{J}_{n+1}\boldsymbol{\omega}_{n+1} - \mathbf{J}_n\boldsymbol{\omega}_n}{\Delta t} + \mathbf{C}^{ang}\frac{\boldsymbol{\omega}_{n+1} + \boldsymbol{\omega}_n}{2} \\ + \mathbf{K}^{ang}\frac{\boldsymbol{\theta}_{n+1} + \boldsymbol{\theta}_n}{2} - \mathbf{M}_{n+1/2}. \quad (29)$$

The corresponding linearized equation system then reads

$$\frac{\partial \mathbf{N}^{ang}}{\partial \boldsymbol{\omega}_{n+1}}\Delta\boldsymbol{\omega}_{n+1} = -\mathbf{N}^{ang}(\boldsymbol{\omega}_{n+1}), \quad (30)$$

with the approximate left-hand side matrix given by

$$\frac{\partial \mathbf{N}^{ang}}{\partial \boldsymbol{\omega}_{n+1}} \approx \frac{1}{\Delta t}\mathbf{J}_{n+1} + \frac{1}{2}\mathbf{C}^{ang} + \frac{1}{2}\mathbf{K}^{ang}\frac{\partial \boldsymbol{\theta}_{n+1}}{\partial \boldsymbol{\omega}_{n+1}}, \quad (31)$$

where the inertia tensor is assumed to not have a strong dependence on the angular velocity. To obtain an explicit expression for the left-had-side matrix, one needs to calculate the derivative $\frac{\partial \boldsymbol{\theta}_{n+1}}{\partial \boldsymbol{\omega}_{n+1}}$. In the case of *planar motion*, it can be shown that

$$\boldsymbol{\omega} = \dot{\boldsymbol{\theta}}. \quad (32)$$

Assuming midpoint integration of the above equation leads to

$$\frac{\partial \boldsymbol{\theta}_{n+1}}{\partial \boldsymbol{\omega}_{n+1}} = \frac{2}{\Delta t}\mathbf{I}, \quad (33)$$

which, in turn, gives

$$\frac{\partial \mathbf{N}^{ang}}{\partial \boldsymbol{\omega}_{n+1}} \approx \frac{1}{\Delta t}\mathbf{J}_{n+1} + \frac{1}{2}\mathbf{C}^{ang} + \frac{\Delta t}{4}\mathbf{K}^{ang}. \quad (34)$$

The matrix-valued discrete residual for the equation governing the evolution of the rotation matrix (see Eq. (11)) may be written as

$$\mathbf{N}^{rot}(\mathbf{R}_{n+1}) = \frac{\mathbf{R}_{n+1} - \mathbf{R}_n}{\Delta t} - \left(\frac{\boldsymbol{\Omega}_{n+1} + \boldsymbol{\Omega}_n}{2}\right)\left(\frac{\mathbf{R}_{n+1} + \mathbf{R}_n}{2}\right). \quad (35)$$

The corresponding linearized equation takes on the form

$$D\mathbf{N}^{rot}\Delta\mathbf{R}_{n+1} = -\mathbf{N}^{rot}(\mathbf{R}_{n+1}), \quad (36)$$

where the left-hand-side matrix $D\mathbf{N}^{rot}$ may be directly inferred from Eq. (35) and takes on the form

$$D\mathbf{N}^{rot} \approx \frac{1}{\Delta t}\mathbf{I} - \frac{\boldsymbol{\Omega}_{n+1} + \boldsymbol{\Omega}_n}{4}, \quad (37)$$

where the spin tensor is assumed to not have a strong dependence on the rotation matrix.

Given all quantities at time level t_n; $\mathbf{d}_n$, $\mathbf{v}_n$, $\mathbf{R}_n$, $\boldsymbol{\omega}_n$ and $\boldsymbol{\theta}_n$, and the half-step values of the external forces $\mathbf{F}_{n+1/2}$ and $\mathbf{M}_{n+1/2}$, we advance the rigid object to the time level t_{n+1} as follows. The residuals of the rigid-object system, $\mathbf{N}^{lin}(\mathbf{u}_{n+1})$, $\mathbf{N}^{ang}(\boldsymbol{\omega}_{n+1})$, and $\mathbf{N}^{rot}(\mathbf{R}_{n+1})$, are driven to zero by solving Eqs. (26), (30), and (36) in a sequential fashion, and repeating the sequence until convergence. Increment of the angular velocity is employed to update the spin tensor for the solution of Eq. (37), while increment of the rotation matrix is employed to update the inertia tensor in Eq. (30). Once converged, the rigid-object solution is transferred to the interface mesh and employed as essential boundary conditions for the fluid-mechanics and mesh-motion problems.

To test the rigid-object algorithm, the convergence of Eq. (30) is studied for a coupled FOI analysis of a coarsely discretized rectangular cylinder. A low natural frequency ($f_N = 0.1$ Hz) is chosen such that the dynamic rigid-body

forces become stiffness-dominated. Fig. 2, showing the convergence rates of the l_2-norm of $\mathbf{N}^{ang}$ for various rotation angles, reveals that the rigid-body formulation exhibits fast convergence. Even for relatively large rotations, the residual is converged to machine precision within a few iterations. The cylinder displaced configuration at the same time levels is shown in Fig. 3.

Remark 1 In the present work, the kinematic constraints employed in all computations result in a planar motion of the bridge deck, and the expression given by Eq. (33) remains valid. In the case of small rotations, approximation of the
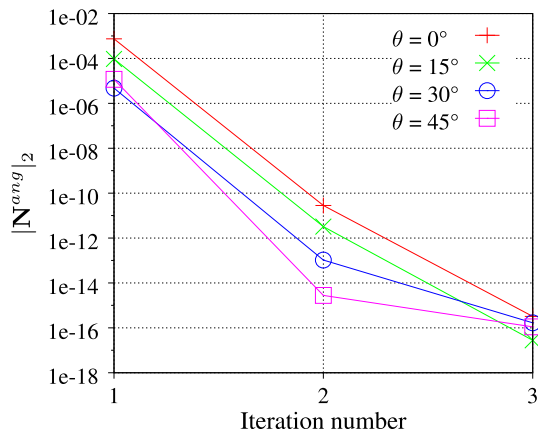
Fig. 2 Convergence in the l_2-norm of the rigid-object angular-momentum-balance residual sampled at various rotation angles

(a) $\theta = 0°$　　　　(b) $\theta = 15°$

(c) $\theta = 30°$　　　　(d) $\theta = 45°$
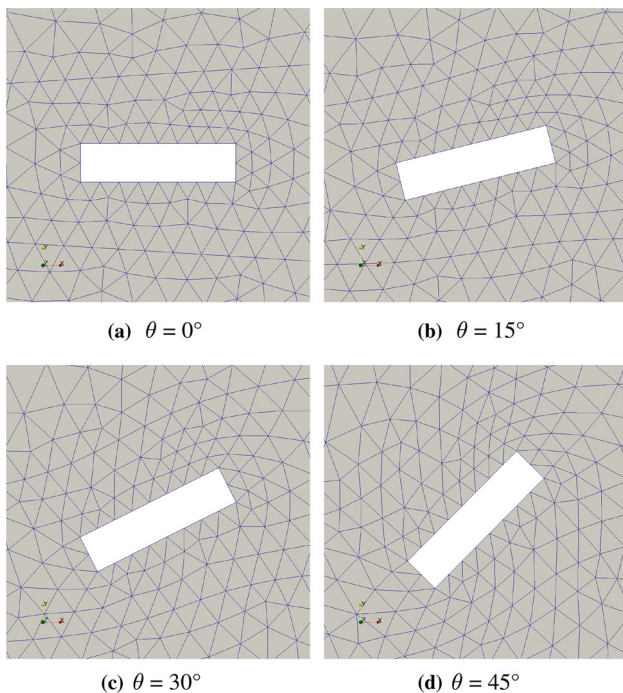
Fig. 3 Object current configurations where convergence of the rigid-body angular-momentum balance is sampled

partial derivative given by Eq. (33) also holds true, and possibly presents a reasonable simplification when deriving the left-hand-side matrix for the general case.

3.4 Time integration of the coupled system

The semi-discrete equations of fluid mechanics (Eq. (18)) and mesh motion (Eq. (23)) are integrated in time using the Generalized-α technique [59,65–67]. A block-iterative approach is employed, where, within a time step, increments of the fluid mechanics, rigid-object, and mesh motion problems are computed sequentially. This approach is efficient for the present application because the added mass effect is not significant.

4 Simplified flutter analysis

In the following section we give a brief presentation of the aeroelastic forces focusing on the application to flutter analysis. For a more detailed description the reader is referred to [68] and references therein. According to strip theory and the definitions and conventions in Fig. 4, the aerodynamic forces acting on a bridge cross section with height H and width B subjected to wind speed U are decomposed into drag, lift and pitching moment, which are denoted D, L and M, respectively. Their corresponding degrees-of-freedom (DOF) are p, h and θ, that match the DOFs in the FOI formulation presented in Sect. 2.2.

Flutter analysis deals with the aerodynamic forces that arise from structural motion, namely, the self-excited forces. Disregarding the lateral component, which in our experimental setup is fixed, the self-excited forces are defined in accordance with [46,69] as

$$L^{se} = \frac{1}{2}\rho U^2 B \left(K H_1^* \frac{\dot{h}}{U} + K H_2^* \frac{B\dot{\theta}}{U} + K^2 H_4^* \frac{h}{B} + K^2 H_3^* \theta \right), \tag{38}$$

$$M^{se} = \frac{1}{2}\rho U^2 B^2 \left(K A_1^* \frac{\dot{h}}{U} + K A_2^* \frac{B\dot{\theta}}{U} + K^2 A_4^* \frac{h}{B} + K^2 A_3^* \theta \right), \tag{39}$$

where ρ is the air density, $K = B\omega/U$ is the reduced frequency of the structural motion, ω being the circular frequency, and H_i^* and A_i^*, $i \in \{1, ..., 4\}$ are the dimensionless flutter derivatives. These are commonly given as functions of the reduced velocity, $V_{red} = K^{-1}$. Superscript *se* stands for "self-excited".

Using matrix notation, the self-excited forces can expressed as

$$\mathbf{q}^{se} = \mathbf{C}_{ae}\dot{\mathbf{r}} + \mathbf{K}_{ae}\mathbf{r}, \tag{40}$$
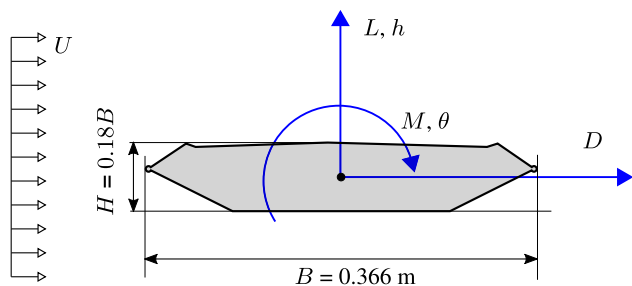
Fig. 4 Aeroelastic forces acting on a 1:50 scale model of the Hardanger bridge

where $\mathbf{q}^{se} = \left[L^{se}, M^{se} \right]^T$ and $\mathbf{r} = [h, \theta]^T$. The matrices $\mathbf{C}_{ae}$ and $\mathbf{K}_{ae}$ are commonly recognized as aerodynamic damping and stiffness, respectively, and are given by

$$\mathbf{C}^{ae} = \frac{1}{2}\rho U K \begin{bmatrix} H_1^* & B H_2^* \\ B A_1^* & B^2 A_2^* \end{bmatrix}, \tag{41}$$

and

$$\mathbf{K}^{ae} = \frac{1}{2}\rho U^2 K^2 \begin{bmatrix} H_4^* & B H_3^* \\ B A_4^* & B^2 A_3^* \end{bmatrix}. \tag{42}$$

Given the still-wind mass, damping, and stiffness matrices, $\mathbf{M}_0$, $\mathbf{C}_0$ and $\mathbf{K}_0$, respectively, dynamic equilibrium of the aeroelastic system is then given by

$$\mathbf{M}_0 \mathbf{G}_{\ddot{\mathbf{r}}}(\omega) + \left(\mathbf{C}_0 - \mathbf{C}^{ae}(U, \omega) \right) \mathbf{G}_{\dot{\mathbf{r}}}(\omega)$$
$$+ \left(\mathbf{K}_0 - \mathbf{K}^{ae}(U, \omega) \right) \mathbf{G}_{\mathbf{r}}(\omega) = \mathbf{G}_{\mathbf{q}}(\omega). \tag{43}$$

Here, $\mathbf{G}_{\ddot{\mathbf{r}}}(\omega)$, $\mathbf{G}_{\dot{\mathbf{r}}}(\omega)$ and $\mathbf{G}_{\mathbf{r}}(\omega)$ are the Fourier transforms (in time) of the acceleration, velocity, and displacement response, respectively. $\mathbf{G}_{\mathbf{q}}(\omega)$ is the Fourier transform of the remaining dynamic forces acting on the system, which include buffeting forces as an important contribution.

The stability of the second-order system with $N = 2$ still-air vibration modes in Eq. (43) is governed by the eigenvalue problem

$$\left(\lambda_n^2 \mathbf{M}_0 + \lambda_n \left(\mathbf{C}_0 - \mathbf{C}^{ae}(U, \omega) \right) \right.$$
$$\left. + \left(\mathbf{K}_0 - \mathbf{K}^{ae}(U, \omega) \right) \right) \boldsymbol{\Phi}_n = 0, \quad n = 1, 2, ...2N. \tag{44}$$

The solution of Eq. (44) gives $2N$ eigenvalues $\lambda_n = \mu_n + i\omega_n$ and eigenvectors $\boldsymbol{\Phi}_n$, and takes the form

$$\mathbf{r}(t) = \sum_{n=1}^{2N} \boldsymbol{\Phi}_n \exp\left((\mu_n + i\omega_n)t \right). \tag{45}$$

To ensure dynamic stability, the real parts μ_n of all eigenvalues should be negative, leading to a decaying response. On the other hand, if any complex eigenvalues have a positive

real part, Eq. (45) exhibit exponential divergence, which is recognized as flutter. The onset of flutter, or the critical wind speed, U_{crit}, occurs at the lowest wind speed for which the real part of λ_n switches sign. Its corresponding eigenvector then represents the flutter mode.

5 Experimental and computational setup

In what follows, we describe the experimental setup and test strategy for the free-vibration wind tunnel experiments performed in this work, and the analysis setup for the numerical simulations. The considered bridge sectional model is a 1:50 scale model of the Hardanger bridge, which is representative of many modern bridge sections. Its aerodynamic performance has also been studied earlier in [2,26,47,68]. We follow the *modus operandi* for most such experiments (see [70] and references therein), using coherent scaling of the dimensions and masses of the bridge section and constant ratio between the first heaving and torsional mode.

Although the forced-vibration method is often preferred to assess the aerodynamic performance due its repeatability and simplified parameter identification procedures, the free-vibration method is still commonly used as a verification tool.

5.1 The free-vibration rig

A schematic 2D view of the free-vibration rig is shown in Fig. 5. The sectional model is suspended vertically via rotation arms with a leverage that gives the targeted frequency ratio. In the horizontal direction the rig is pretensioned with lightweight wires, which are sufficiently long to reduce the geometrical stiffness contribution to a minimum. Additional masses to the center bar and rotation arm are introduced to achieve the proper mass scalings. Figure 6 shows the section installed in the wind tunnel.

5.2 Instrumentation

Load cells (AEP Type TS 25 kg) measure the vertical spring forces. From these, we estimate the displacements via relations determined from separate calibration tests of each spring and static measurements of the installed section. From the displacements in each of the springs we easily compute the motions of the sectional model.

To monitor the pretensioning and drag component, load cells are also installed at the upwind horizontal suspension (AEP Type TCA 5 kg). For signal acquisition and analysis we use HBM Quantum X and Catman software.
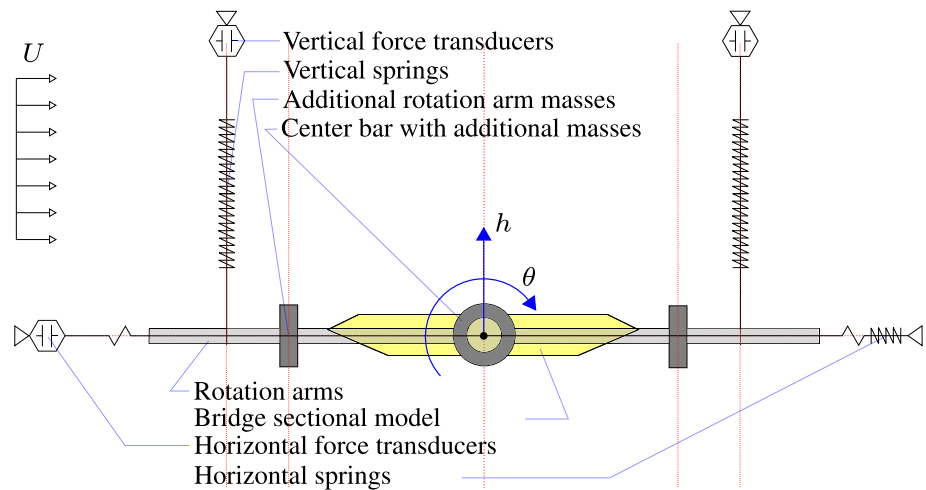
5.3 Test strategy

In order to study the aerodynamic contributions, we need a precise estimation of the system properties in still-wind. We base the system identification on known masses and eigenfrequencies. Thus we also include the geometrical stiffness from the horizontal pretension. As the inertia cannot be calculated without notable uncertainties, we use a system perturbation technique that involves adding a known amount of inertia to the rotation arm and measuring the change in frequency. Damping is estimated by a logarithmic decrement.

The identified system properties, and the corresponding full scale quantities, are summarized in Table 1. The damping ratios vertically and torsionally are read from single-frequency experiments at amplitudes of $h = 15$ mm and $\theta = 3°$, respectively. The full-scale data are taken from [68], and represents the modal quantities of the first symmetrical heaving and torsional modes. The experimental setup renders mass and inertia scaling factors of 50.0^2 and 47.6^4, respectively, which plainly satisfy the geometric scaling.

According to Eq. (44), the flutter wind speed is estimated to be $U_{crit} = 8.16$ and 7.48 m/s using the numerically and experimentally determined aerodynamic derivatives reported in [26] and [45], respectively.

In this work we consider the still-wind case, as well as wind speeds of approximately 25, 50 100% of U_{crit}.

5.4 Analysis setup

The computational domain is taken as a box that represents a 0.25 m-wide slice of the wind tunnel, spanning a distance of $3B$ upwind and $8B$ downwind from the bridge-deck centroid. The height is set to 1.815 m, same as the wind-tunnel physical dimension. For the boundary conditions a uniform wind speed U is prescribed on the inflow surface. The walls and
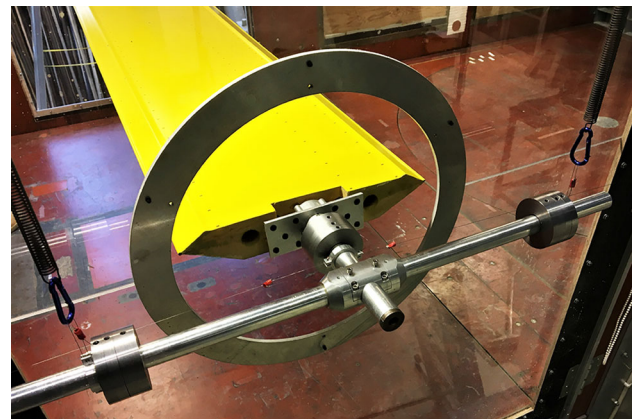
Fig. 6 Sectional model installed for free-vibration experiments. The center bar extends through the circular hole so that most of the apparatus is outside the wind-tunnel walls. Note the horizontal suspension attached to the center bar

transverse boundaries are constrained with no-penetration, and the outflow boundary is traction-free. The bridge deck surface is constrained with weakly-enforced no-slip BC. For the rigid-body, only the vertical-displacement and rotation DOFs are kept active in all simulations.

The air density is set to $\rho = 1.225$ kg/m^3 and the dynamic viscosity is set to $\mu = 1.7894 \times 10^{-5}$ kg/ms. The time step is set to $\Delta t = 0.001B/U$, which keeps the maximum Courant number at 2.5 or lower.

For discretization we use unstructured linear tetrahedra and triangular prisms, with local refinement near the bridge deck and in its wake region. To guarantee good mesh quality near the bridge deck, we adopt the Solid-Extension Mesh Moving Technique (SEMMT) [71,72]. In this approach, structured layers of prismatic elements undergo the same rigid-body motion as the bridge deck itself, which preserves the original mesh quality near the bridge deck in the moving-mesh simulations. Moreover, this approach signifi-

Table 1 Still-air system properties for the experimental setup

Property		Experiment	Full scale	
Mass	m	5.120	12820	kg/m
Inertia	I_θ	0.08295	426 000	kgm^2/m
Vertical eigenfrequency	ω_h	5.0087	0.89	rad/s
Torsional eigenfrequency	ω_θ	12.6351	2.23	rad/s
Frequency ratio		2.52	2.51	–
Vertical structural damping ratio	ζ_h	3.8×10^{-3}	6.0×10^{-3}	–
Torsional structural damping ratio	ζ_θ	1.2×10^{-3}	5.0×10^{-3}	–

cantly reduces the cost of the mesh-motion problem. Fig. 7 shows an outline of the computational domain and a detailed view of the bridge deck that shows the boundary-layer elements and indicates the general mesh density.

The total number of nodes in the model is 644,000, and the computations are performed in a parallel environment described in [73] using 256 compute cores.

(a)

(b)
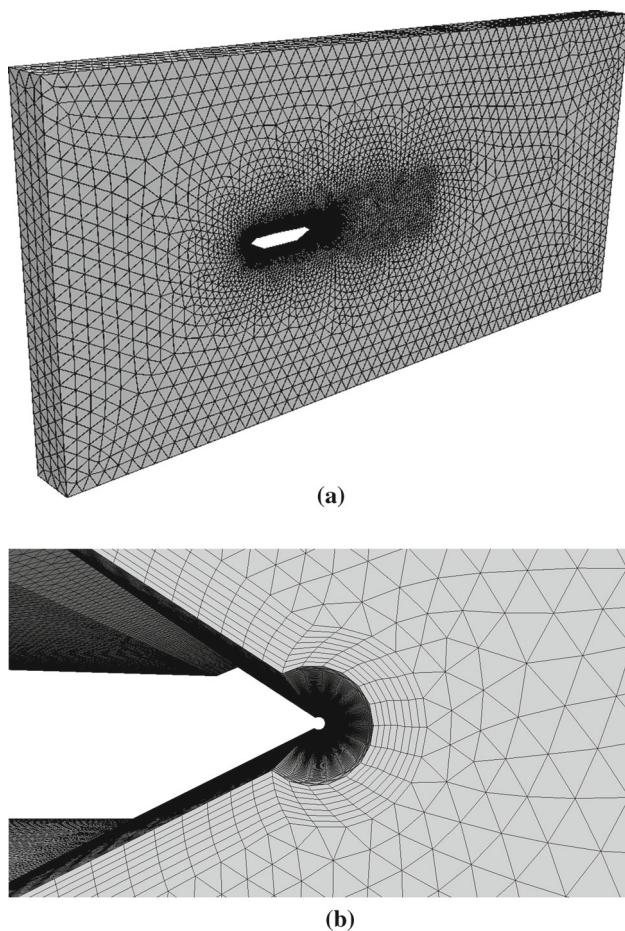
Fig. 7 Problem mesh. **a** Full computational domain, **b** zoom on the leading edge

6 Results and discussion

In this section we present the numerical results. Our main goal is to test if FOI formulation is able to capture the effect of the aerodynamic forces on the eigenfrequencies and damping. Especially the latter is of particular interest in the analysis of aerodynamic stability. The damping is represented by the logarithmic decrement, δ, whose relationship to the damping ratio is given by $\delta = 2\pi\zeta/\sqrt{1-\zeta^2}$. A selection of videos and visualizations from the experiments and simulations are available at our Youtube channel "Structural Dynamics NTNU".

6.1 Still-wind simulations

To test the formulation and assess the still-wind damping and stiffness, free decay simulations are performed for the vertical and torsional degrees-of-freedom. The system properties determined from such experiments are commonly referred to as structural properties, however, as the aerodynamic loads are nonzero, also these have an aerodynamic contribution which can be quantified by the simulations.

The system masses are taken from Table 1. To account for the aerodynamic stiffness contribution (which would slow down the structural motion according to Eq. (44)), the eigenfrequencies are set to $\omega_h = 5.072$ and $\omega_\theta = 12.675$ rad/s. This small adjustment is based on the phase-lag from a one-period test simulation. Similarly, the structural, or external damping ratios are set to $\zeta_h = 5 \times 10^{-4}$ and $\zeta_\theta = 7 \times 10^{-4}$. For the initial condition the bridge section is ramped up to $h = 20$ mm and $\theta = 3°$ from its equilibrium position for the two simulations, respectively. For stability reasons, the inflow velocity is set to small value of $U = 0.1$ m/s.

Fig. 8 shows the displacement time histories for the two simulations together with the corresponding wind tunnel experiments. To assess the aerodynamic contribution, the oscillation envelopes of the mechanical damping are shown in the same plot. A summary of the results also follows in Table 2. The almost indistinguishable results prove that with the proper choice of structural stiffnesses and damping the formulation captures the still-wind behavior with excellent
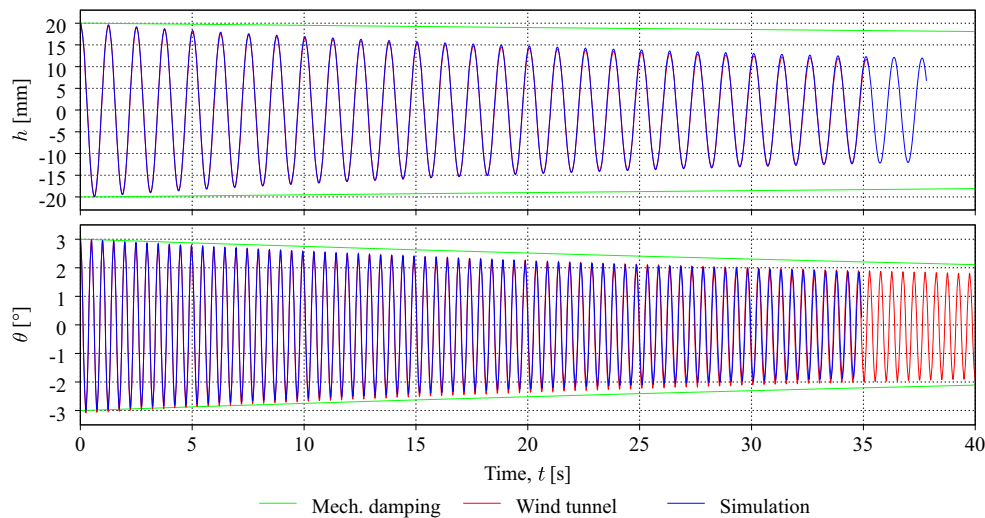
Fig. 8 Displacement of the bridge deck centroid for still-wind simulations with the vertical motion (top) and the torsional motion (bottom) actuated. Wind-tunnel experimental data are aligned at $t = 0$

Table 2 A summary of the experimentally and numerically obtained eigenfrequencies and damping ratios for various wind speeds

	Still-wind		$U = 1.75$ m/s		$U = 3.85$ m/s		$U = 8.16$ m/s	
	Exp.	Sim.	Exp.	Sim.	Exp.	Sim.	Exp.	Sim.
Vertical eigenfrequency, ω_h (rad/s)	5.009	4.984	5.086	5.118	5.161	5.258	9.795	9.084
Torsional eigenfrequency, ω_θ (rad/s)	12.654	12.595	12.570	12.566	12.176	12.103	9.795	9.084
Vertical damping, ζ_h (%)	0.30	0.26	2.50	2.50	7.27	8.06	0.00	
Torsional damping, ζ_θ (%)	0.09	0.11	0.24	0.33	0.69	1.02	0.00	

+ Wind tunnel   ⊙ Simulation
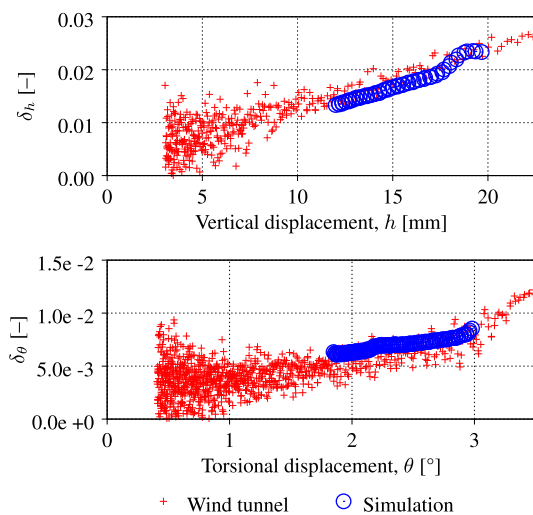
Fig. 9 Logarithmic decrement with respect to the displacement amplitude for the vertical (top) and torsional (bottom) motion in still wind

accuracy. We also observe that still-wind vertical damping is dominated by the aerodynamic forces.

Figure 9 shows the logarithmic decrement with respect to the displacement amplitude for the two simulations. First, we notice that the damping is extremely low for the still-

wind condition. Further, it appears to vary linearly with the vibration amplitude, a phenomenon which is also reported in [47]. This behavior is very precisely captured in the simulations. The amplitude-dependent damping arises from correlation between the aerodynamic forces and structural velocity. Because vertical motion induces more vorticity, and, consequently, higher energy dissipation than the pitching motion, as can be seen from the snapshots in Fig. 10, it is also subjected to more aerodynamic damping.

6.2 In-wind simulations

Using the same system properties we now perform free-vibration simulations at wind speeds $U = 1.75$ and 3.85 m/s, where the aeroelastic forces are no longer negligible. The same analysis setup is used as described in Sect. 5.4.

Figures 11 and 12 show displacement time histories for $U = 1.75$ and $U = 3.85$ m/s, respectively, and their corresponding damping ratios are shown in Figs. 13 and 14. Table 2 summarizes the results.

For the vertical displacement DOF, we capture its magnitude very well. Invariance of the aerodynamic damping with respect to the displacement magnitude is also captured with excellent accuracy. Good results are likewise obtained for the

(a) $t = t_0$ **(b)** $t = t_0 + T/4$ **(c)** $t = t_0 + T/2$

(d) $t = t_0$ **(e)** $t = t_0 + T/4$ **(f)** $t = t_0 + T/2$
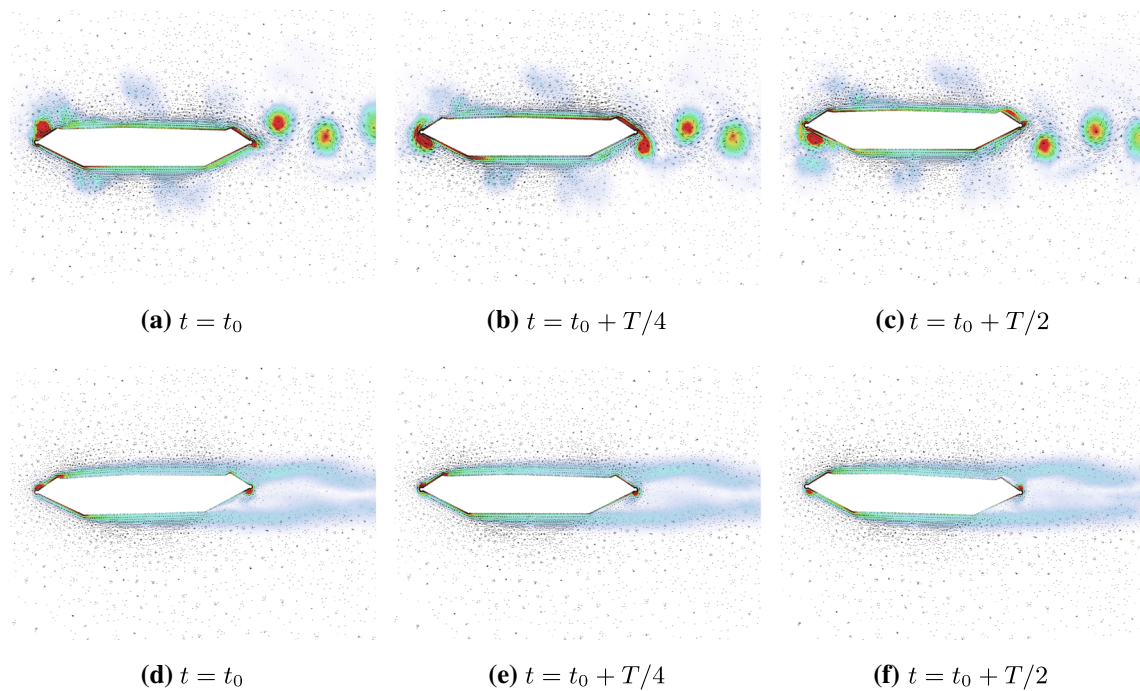
Fig. 10 Snapshots of vorticity contours and velocity vectors for the vertical (top) and pitching (bottom) motion in still wind. Here t_0 represents the time level at a lower peak displacement, and $T = 2\pi/\omega$ is the period
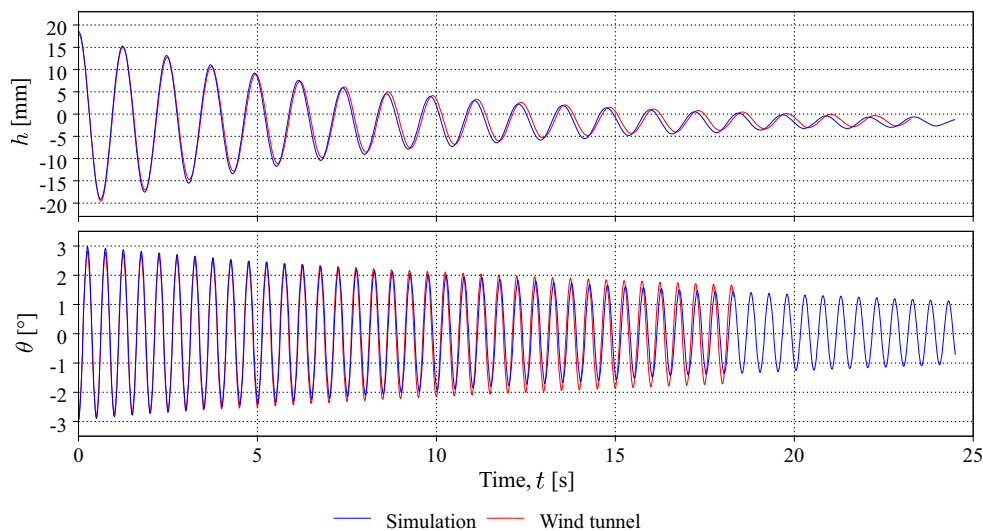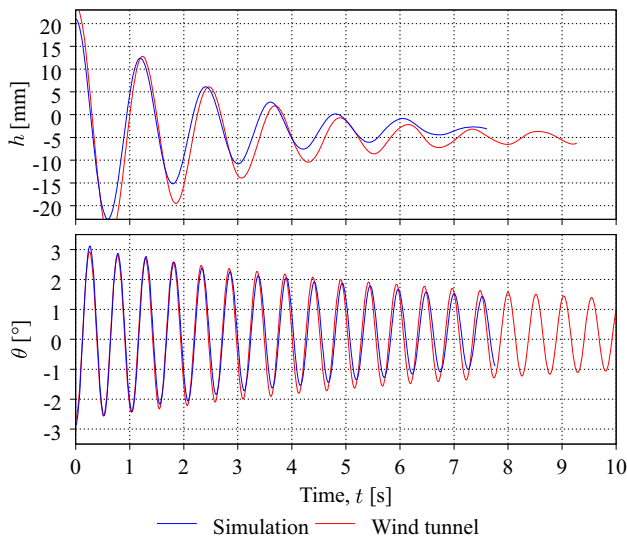

Fig. 11 Displacement time series of the bridge deck subjected to a wind speed of $U = 1.75$ m/s and actuating the heaving (top) and pitching (bottom) mode. Wind-tunnel experimental data are aligned at $t = 0$

torsional DOF, however, the simulation predicts higher aero-dynamic damping. This observation corresponds with the overestimation of the A_1^* and A_2^* aerodynamic derivatives our earlier work [26]. It should be remarked that, already at 25% of the flutter wind speed, the vertical-displacement aerodynamic damping is one order of magnitude higher than the still-wind damping.
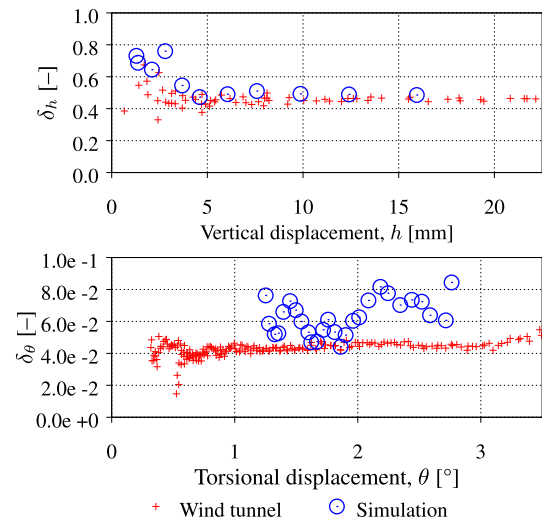
The magnitude of the aerodynamic stiffness is slightly overestimated in both DOFs, however, its evolution with the wind speed agrees very well with the experiments.

From the time histories, most prominently for $U = 3.85$ m/s, we notice a difference in the mean displacements. This indicates that the simulations produce different absolute val-ues of the aerodynamic lift and pitching moments. However, other sources of errors, e.g. inaccurate alignment of the sec-tional model, are also present. Since the mean values are removed in the analysis of motion-induced forces and flut-ter, this issue is not further addressed in this work.
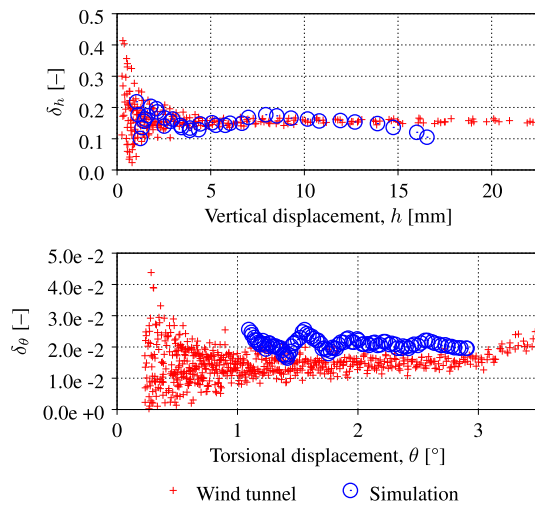
Remark 2 We want to emphasize that although the heaving and pitching time series are hitherto drawn together, they are

Fig. 12 Displacement time series of the bridge deck subjected to a wind speed of $U = 3.85$ m/s and actuating the heaving (top) and pitching (bottom) mode. Wind-tunnel experimental data are aligned at $t = 0$

Fig. 13 Logarithmic decrement with respect to the displacement amplitude for the vertical (top) and torsional (bottom) motion for $U = 1.75$ m/s

Fig. 14 Logarithmic decrement with respect to the displacement amplitude for the vertical (top) and torsional (bottom) motion for $U = 3.85$ m/s
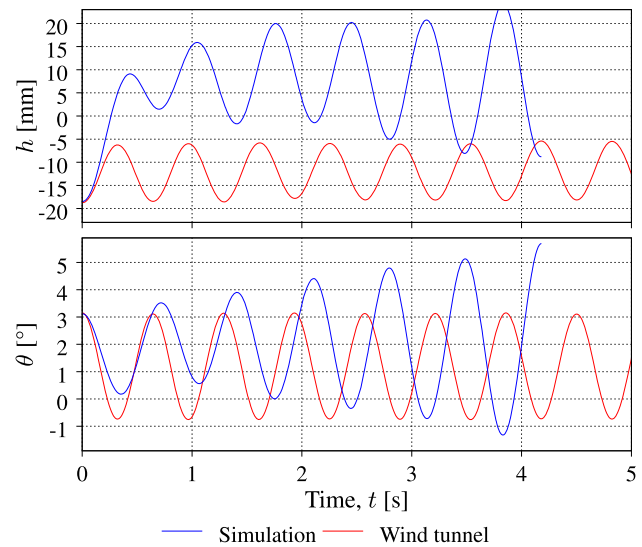
Fig. 15 Time histories of the vertical displacement and rotation angle

6.3 Flutter

Combining the system properties in Table 1 and the aerodynamic derivatives from forced-vibration wind tunnel experiments [45], solution of the eigenvalue problem Eq. (44) gives $U_{crit} = 7.48$ m/s and a critical vibration frequency of $\omega_{cr} = 10.11$ rad/s. From the numerically obtained aerodynamic derivatives reported in [26], the corresponding results are $U_{crit} = 8.16$ m/s and $\omega_{cr} = 8.92$ rad/s.

From the free-vibration experiments we obtain $U_{crit} = 8.16$ m/s and $\omega_{cr} = 9.80$ rad/s. Using the same wind velocity in the simulations we obtain a diverging response, which indicates that we are above, but close to U_{crit}. Time histories are shown in Fig. 15, and it is evident that the simulation
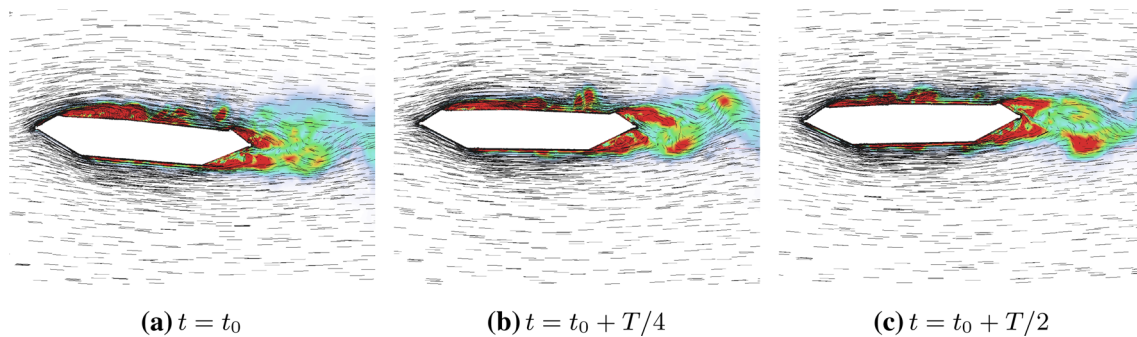
computed sequentially. The DOF which is not actuated is still active, however, it undergoes vanishingly small excitation due to the narrow-banded nature of the aerodynamic forces which act in the region of the dominating motion.

Remark 3 It should be noted that the reported eigenfrequencies are in fact the damped natural frequencies. The effect of damping on the vibration frequency is, however, vanishingly small compared to the contribution from the aerodynamic stiffness.

(a) $t = t_0$ **(b)** $t = t_0 + T/4$ **(c)** $t = t_0 + T/2$

Fig. 16 Snapshots of vorticity contours and velocity vectors for the flutter simulation. Here t_0 represents the time level at a lower peak displacement, and $T = 2\pi/\omega$ is the period

gives a very accurate representation of the flutter mode in terms of the frequency ($\omega_{cr} = 9.084$) and mode shape. A visualization of the flutter mode is given in Fig. 16, from where we see that the bridge deck is undergoing a pitching motion with a center of rotation very close to the leading edge.

The good correspondence between the predicted flutter characteristics obtained numerically by the forced-vibration method in [26] and the experimentally obtained flutter herein provides additional validation of the fluid mechanics part of the computational framework employed in this work.

7 Conclusions

This paper presents an FOI modeling approach with a coupling between the ALE-VMS formulation for fluid dynamics and equations of a rigid object. The rigid-object formulation is augmented with external stiffness and damping, which makes it suitable for many engineering applications, such as vibration analysis of bridge decks.

For the rigid-body formulation we have proposed a modified time-integration algorithm, in which a linear relationship between the Euler-angle time derivative and angular velocity vector is assumed in the expression for the tangent matrix employed in the rigid-object algorithm.

The resulting formulation was employed to simulate the free-vibration wind-tunnel experiments of the 1:50 scale model of the Hardanger bridge section. The latter were also carried out as part of this work. The results show that the FOI formulation reproduces the aeroelastic behavior with excellent accuracy. Tests at different wind speeds reveal the evolution of aerodynamic stiffness and damping, where especially the latter is heavily influenced by the aerodynamic forces. Numerical simulation at the flutter stability limit also show that the FOI formulation captures the critical wind speed and the corresponding vibration mode.

In the context of bridge engineering, free-vibration wind-tunnel experiments often serve to validate their corresponding forced-vibration experiments. Analogously, this work serves as a validation of the forced-vibration computational framework presented by the same authors in [26], which gave flutter characterization that is in very good agreement well with the free-vibration results obtained herein. Besides validation of forced vibrations, the authors believe that the computational framework presented herein can be a valuable tool to quickly assess the more general aeroelastic performance of bridge sections, which is especially important for the front-end engineering design.

References

1. Akkerman I, Bazilevs Y, Benson DJ, Farthing MW, Kees CE (2012) Free-surface flow and fluid-object interaction modeling with emphasis on ship hydrodynamics. J Appl Mech 79(1):010905. https://doi.org/10.1115/1.4005072
2. Takizawa K, Bazilevs Y, Tezduyar TE, Hsu M-C, Øiseth O, Mathisen KM, Kostov N, McIntyre S (2014) Engineering analysis and design with ALE-VMS and space-time methods. Arch Comput Methods Eng 21(4):481–508. https://doi.org/10.1007/s11831-014-9113-0
3. Tezduyar TE, Behr M, Mittal S, Liou J (1992) A new strategy for finite element computations involving moving boundaries and interfaces. The deforming-spatial-domain/space-time procedure: II. Computation of free-surface flows, two-liquid flows, and flows with drifting cylinders. Comput Methods Appl Mech Eng 94(3):353–371. https://doi.org/10.1016/0045-7825(92)90060-W
4. Mittal S, Tezduyar TE (1992) A finite element study of incompressible flows past oscillating cylinders and aerofoils. Int J Numer Methods Fluids 15(9):1073–1118. https://doi.org/10.1002/fld.1650150911

5. Tezduyar TE (2001) Finite element methods for flow problems with moving boundaries and interfaces. Arch Comput Methods Eng 8:83–130. https://doi.org/10.1007/BF02897870

6. Ed Akin J, Tezduyar TE, Ungor M (2007) Computation of flow problems with the mixed interface-tracking/interface-capturing technique (MITICT). Comput Fluids 36(1):2–11. https://doi.org/10.1016/j.compfluid.2005.07.008

7. Akkerman I, Bazilevs Y, Kees CE, Farthing MW (2011) Isogeometric analysis of free-surface flow. J Comput Phys 230(11):4137–4152. https://doi.org/10.1016/j.jcp.2010.11.044

8. Akkerman I, Dunaway J, Kvandal J, Spinks J, Bazilevs Y (2012) Toward free-surface modeling of planing vessels: simulation of the Fridsma hull using ALE-VMS. Comput Mech 50(6):719–727. https://doi.org/10.1007/s00466-012-0770-2

9. Kees CE, Akkerman I, Farthing MW, Bazilevs Y (2011) A conservative level set method suitable for variable-order approximations and unstructured meshes. J Comput Phys 230(12):4536–4558. https://doi.org/10.1016/j.jcp.2011.02.030

10. R. P. Selvam, S. Govindaswamy, H. Bosch, Aeroelastic analysis of bridges using FEM and moving grids, Wind and Structures 5 (2_3_4) (2002) 257–266. https://doi.org/10.12989/was.2002.5.2_3_4.257. http://koreascience.or.kr/journal/view.jsp?kj=KJKHCF&py=2002&vnc=v5n2_3_4&sp=257

11. Frandsen JB (2004) Numerical bridge deck studies using finite elements. Part I: Flutter. J Fluids Struct 19(2):171–191. https://doi.org/10.1016/j.jfluidstructs.2003.12.005

12. Bazilevs Y, Hsu M-C, Takizawa K, Tezduyar TE (2012) ALE-VMS and ST-VMS methods for computer modeling of wind-turbine rotor aerodynamics and fluid-structure interaction. Math Models Methods Appl Sci 22(supp02):1230002. https://doi.org/10.1142/S0218202512300025

13. Bazilevs Y, Takizawa K, Tezduyar TE (2013) Challenges and directions in computational fluid-structure interaction. Math Models Methods Appl Sci 23(02):215–221. https://doi.org/10.1142/S0218202513400010

14. Bazilevs Y, Takizawa K, Tezduyar TE, Hsu M-C, Kostov N, McIntyre S (2014) Aerodynamic and FSI analysis of wind turbines with the ALE-VMS and ST-VMS methods. Arch Comput Methods Eng 21(4):359–398. https://doi.org/10.1007/s11831-014-9119-7

15. Bazilevs Y, Takizawa K, Tezduyar TE (2015) New directions and challenging computations in fluid dynamics modeling with stabilized and multiscale methods. Math Models Methods Appl Sci 25(12):2217–2226. https://doi.org/10.1142/S0218202515020029

16. Bazilevs Y, Korobenko A, Yan J, Pal A, Gohari SMI, Sarkar S (2015) ALEVMS formulation for stratified turbulent incompressible flows with applications. Math Models Methods Appl Sci 25(12):2349–2375. https://doi.org/10.1142/S021820251540011

17. Bazilevs Y, Michler C, Calo VM, Hughes TJR (2007) Weak Dirichlet boundary conditions for wall-bounded turbulent flows. Comput Methods Appl Mech Eng 196(49–52):4853–4862. https://doi.org/10.1016/j.cma.2007.06.026

18. Bazilevs Y, Hughes TJR (2007) Weak imposition of Dirichlet boundary conditions in fluid mechanics. Comput Fluids 36(1):12–26. https://doi.org/10.1016/j.compfluid.2005.07.012

19. Bazilevs Y, Akkerman I (2010) Large eddy simulation of turbulent Taylor–Couette flow using isogeometric analysis and the residual-based variational multiscale method. J Comput Phys 229(9):3402–3414. https://doi.org/10.1016/j.jcp.2010.01.008

20. Bazilevs Y, Tezduyar TE (2013) Computational fluid structure interaction methods and application. Wiley, Hoboken. https://doi.org/10.1002/9781118483565

21. Hsu M-C, Akkerman I, Bazilevs Y (2012) Wind turbine aerodynamics using ALEVMS: validation and the role of weakly enforced boundary conditions. Comput Mech 50(4):499–511. https://doi.org/10.1007/s00466-012-0686-x

22. Hsu M-C, Kamensky D, Bazilevs Y, Sacks MS, Hughes TJR (2014) Fluid structure interaction analysis of bioprosthetic heart valves: significance of arterial wall deformation. Comput Mech 54(4):1055–1071. https://doi.org/10.1007/s00466-014-1059-4

23. Yan J, Korobenko A, Deng X, Bazilevs Y (2016) Computational free-surface fluid structure interaction with application to floating offshore wind turbines. Computers & Fluids 141:155–174. https://doi.org/10.1016/j.compfluid.2016.03.008. http://linkinghub.elsevier.com/retrieve/pii/S0045793016300536

24. Scotta R, Lazzari M, Stecca E, Cotela J, Rossi R (2016) Numerical wind tunnel for aerodynamic and aeroelastic characterization of bridge deck sections. Comput Struct 167:96–114. https://doi.org/10.1016/j.compstruc.2016.01.012

25. Helgedagsrud TA, Mathisen KM, Bazilevs Y, Øiseth O, Korobenko A (2017) Using ALE-VMS to compute wind forces on moving bridge decks. In: Skallerud B, Andersson HI (eds.) Proceedings of MekIT'17 ninth national conference on computational mechanics, CMIME, Barcelona, Spain, pp. 169–189

26. Helgedagsrud TA, Bazilevs Y, Korobenko A, Mathisen KM, Øiseth OA (2018) Using ALE-VMS to compute aerodynamic derivatives of bridge sections, Computers Fluids, published online. https://doi.org/10.1016/j.compfluid.2018.04.037. http://linkinghub.elsevier.com/retrieve/pii/S0045793018302330

27. Takizawa K, Tezduyar TE (2011) Multiscale spacetime fluid structure interaction techniques. Comput Mech 48(3):247–267. https://doi.org/10.1007/s00466-011-0571-z

28. Takizawa K, Tezduyar TE (2012) Space-time fluid-structure interaction methods. Math Models Methods Appl Sci 22(supp02):1230001. https://doi.org/10.1142/S0218202512300013

29. Takizawa K, Tezduyar TE, Buscher A, Asada S (2014) Spacetime interface-tracking with topology change (ST-TC). Comput Mech 54(4):955–971. https://doi.org/10.1007/s00466-013-0935-7

30. Takizawa K, Tezduyar TE, Buscher A (2015) Spacetime computational analysis of MAV flapping-wing aerodynamics with wing clapping. Comput Mech 55(6):1131–1141. https://doi.org/10.1007/s00466-014-1095-0

31. Takizawa K, Tezduyar TE, Buscher A, Asada S (2014) Spacetime fluid mechanics computation of heart valve models. Comput Mech 54(4):973–986. https://doi.org/10.1007/s00466-014-1046-9

32. Takizawa K, Tezduyar TE, Terahara T, Sasaki T (2017) Heart valve flow computation with the integrated SpaceTime VMS. Slip interface, topology change and isogeometric discretization methods. Comput Fluids 158:176–188. https://doi.org/10.1016/j.compfluid.2016.11.012. http://linkinghub.elsevier.com/retrieve/pii/S0045793016303681

33. Takizawa K, Tezduyar TE, Kuraishi T, Tabata S, Takagi H (2016) Computational thermo-fluid analysis of a disk brake. Comput Mech 57(6):965–977. https://doi.org/10.1007/s00466-016-1272-4

34. Takizawa K, Tezduyar TE, Hattori H (2017) Computational analysis of flow-driven string dynamics in turbomachinery. Comput Fluids 142:109–117. https://doi.org/10.1016/j.compfluid.2016.02.019

35. Takizawa K, Tezduyar TE, Otoguro Y, Terahara T, Kuraishi T, Hattori H (2017) Turbocharger flow computations with the space-time isogeometric analysis (ST-IGA). Comput Fluids 142:15–20. https://doi.org/10.1016/j.compfluid.2016.02.021

36. Otoguro Y, Takizawa K, Tezduyar TE (2017) Spacetime VMS computational flow analysis with isogeometric discretization and a general-purpose NURBS mesh generation method. Comput Fluids 158:189–200. https://doi.org/10.1016/j.compfluid.2017.04.017

37. Takizawa K, Tezduyar TE, Asada S, Kuraishi T (2016) SpaceTime method for flow computations with slip interfaces and topology changes (ST-SI-TC). Comput Fluids 141:124–134. https://doi.org/10.1016/j.compfluid.2016.05.006

38. Šarkić A, Fisch R, Höffer R, Bletzinger KU (2012) Bridge flutter derivatives based on computed, validated pressure fields. J Wind Eng Ind Aerodyn 104–106:141–151. https://doi.org/10.1016/j.jweia.2012.02.033

39. Brusiani F, Miranda SD, Patruno L, Ubertini F, Vaona P (2013) On the evaluation of bridge deck flutter derivatives using RANS turbulence models. J Wind Eng 119:39–47

40. Bai Y, Yang K, Sun D, Zhang Y, Kennedy D, Williams F, Gao X (2013) Numerical aerodynamic analysis of bluff bodies at a high Reynolds number with three-dimensional CFD modeling. Sci China Phys Mech Astron 56(2):277–289. https://doi.org/10.1007/s11433-012-4982-4

41. de Miranda S, Patruno L, Ubertini F, Vairo G (2014) On the identification of flutter derivatives of bridge decks via RANS turbulence models: Benchmarking on rectangular prisms. Eng Struct 76:359–370. https://doi.org/10.1016/j.engstruct.2014.07.027

42. Nieto F, Owen JS, Hargreaves DM, Hernández S (2015) Bridge deck flutter derivatives: efficient numerical evaluation exploiting their interdependence. J Wind Eng Ind Aerodyn J 136:138–150

43. Patruno L (2015) Accuracy of numerically evaluated flutter derivatives of bridge deck sections using RANS: effects on the flutter onset velocity. Eng Struct 89:49–65. https://doi.org/10.1016/j.engstruct.2015.01.034

44. Diana G, Rocchi D, Belloli M (2015) Wind tunnel : a fundamental tool for long-span bridge design. Struct Infrastruct Eng Maint Manag Life Cycle Des Perform 11(4):533–555. https://doi.org/10.1080/15732479.2014.951860

45. Siedziako B, Øiseth O, Rønnquist A (2017) An enhanced forced vibration rig for wind tunnel testing of bridge deck section models in arbitrary motion. J Wind Eng Ind Aerodyn 164:152–163. https://doi.org/10.1016/j.jweia.2017.02.011

46. Scanlan RH, Tomko J (1971) Airfoil and bridge deck flutter derivatives. J Eng Mech Div 97(6):1717–1737

47. Svend Ole Hansen APS, The Hardanger bridge: static and dynamic wind tunnel tests with a section model. Technical report, prepared for Norwegian Public Roads Administration, Tech. rep. (2006)

48. Hughes TJR, Liu WK, Zimmermann TK (1981) Lagrangian-Eulerian finite element formulation for incompressible viscous flows. Comput Methods Appl Mech Eng 29(3):329–349. https://doi.org/10.1016/0045-7825(81)90049-9

49. Hughes T, Tezduyar T (1984) Finite element methods for first-order hyperbolic systems with particular emphasis on the compressible euler equations. Comput Methods Appl Mech Eng 45(1–3):217–284. https://doi.org/10.1016/0045-7825(84)90157-9

50. Hughes TJ, Franca LP, Balestra M (1986) A new finite element formulation for computational fluid dynamics. : V. Circumventing the babuška-brezzi condition: a stable Petrov-Galerkin formulation of the stokes problem accommodating equal-order interpolations. Comput Methods Appl Mech Eng 59(1):85–99. https://doi.org/10.1016/0045-7825(86)90025-3

51. Tezduyar T, Park Y (1986) Discontinuity-capturing finite element formulations for nonlinear convection-diffusion-reaction equations. Comput Methods Appl Mech Eng 59(3):307–325. https://doi.org/10.1016/0045-7825(86)90003-4

52. Tezduyar TE, Osawa Y (2000) Finite element stabilization parameters computed from element matrices and vectors. Comput Methods Appl Mech Eng 190:411–430. https://doi.org/10.1016/S0045-7825(00)00211-5

53. Tezduyar TE (2003) Computation of moving boundaries and interfaces and stabilization parameters. Int J Numer Methods Fluids 43(5):555–575. https://doi.org/10.1002/fld.505

54. Hughes TJR, Sangalli G (2007) Variational multiscale analysis: the fine scale Green's function, projection, optimization, localization, and stabilized methods. SIAM J Numer Anal 45(2):539–557. https://doi.org/10.1137/050645646

55. Hsu M-C, Bazilevs Y, Calo V, Tezduyar T, Hughes T (2010) Improving stability of stabilized and multiscale formulations in flow simulations at small time step. Comput Methods Appl Mech Eng 199(13–16):828–840. https://doi.org/10.1016/j.cma.2009.06.019

56. Takizawa K, Tezduyar TE, Kuraishi T (2015) Multiscale spacetime methods for thermo-fluid analysis of a ground vehicle and its tires. Math Models Methods Appl Sci 25(12):2227–2255. https://doi.org/10.1142/S0218202515400072

57. Takizawa K, Tezduyar TE, Mochizuki H, Hattori H, Mei S, Pan L, Montel K (2015) Spacetime VMS method for flow computations with slip interfaces (ST-SI). Math Models Methods Appl Sci 25(12):2377–2406. https://doi.org/10.1142/S0218202515400126

58. K. Takizawa, T. E. Tezduyar, Y. Otoguro, Stabilization and discontinuity-capturing parameters for spacetime flow computations with finite element and isogeometric discretizations, Comput Mech.published online (2018). https://doi.org/10.1007/s00466-018-1557-x

59. Bazilevs Y, Calo VM, Hughes TJR, Zhang Y (2008) Isogeometric fluid-structure interaction: theory, algorithms, and computations. Comput Mech 43(1):3–37. https://doi.org/10.1007/s00466-008-0315-x

60. Stein K, Tezduyar T, Benney R (2003) Mesh moving techniques for fluid-structure interactions with large displacements. J Appl Mech 70(1):58. https://doi.org/10.1115/1.1530635

61. Tezduyar TE, Behr M, Mittal S, Johnson AA (1992) Computation of unsteady incompressiblke flows and massively parallel implementations. New Methods Transient Anal 246:7–24

62. Tezduyar T, Aliabadi S, Behr M, Johnson A, Mittal S (1993) Parallel finite-element computation of 3D flows. Computer 26(10):27–36. https://doi.org/10.1109/2.237441

63. Johnson A, Tezduyar T (1994) Mesh update strategies in parallel finite element computations of flow problems with moving boundaries and interfaces. Comput Methods Appl Mech Eng 119(1–2):73–94. https://doi.org/10.1016/0045-7825(94)00077-8

64. Hughes TJR, Winget J (1980) Finite rotation effects in numerical integration of rate constitutive equations arising in large-deformation analysis. Int J Numer Methods Eng 15(12):1862–1867. https://doi.org/10.1002/nme.1620151210

65. Jansen KE, Whiting CH, Hulbert GM (2000) A generalized-α method for integrating the filtered Navier-Stokes equations with a stabilized finite element method. Comput Methods Appl Mech Eng 190:305–319

66. Kuhl E, Hulshoff S, de Borst R (2003) An arbitrary lagrangian eulerian finite-element approach for fluid-structure interaction phenomena. Int J Numer Methods Eng 57(1):117–142. https://doi.org/10.1002/nme.749

67. Dettmer WG, Peric D (2006) A computational framework for fluid-structure interaction: finite element formulation and applications. Comput Methods Appl Mech Eng 195:5754–5779

68. Øiseth O, Rönnquist A, Sigbjörnsson R (2010) Simplified prediction of wind-induced response and stability limit of slender long-span suspension bridges, based on modified quasi-steady theory: A case study. J Wind Eng Ind Aerodyn 98(12):730–741. https://doi.org/10.1016/j.jweia.2010.06.009

69. Scanlan RH (1993) Problematics in formulation of wind force models for bridge decks. J Eng Mech 119(7):1353–1375. https://doi.org/10.1061/(ASCE)0733-9399(1993)119:7(1353)

70. Bartoli G, Contri S, Mannini C, Righi M (2009) Toward an improvement in the identification of bridge deck flutter derivatives. J Eng Mech 135(8):771–785. https://doi.org/10.1061/(ASCE)0733-9399(2009)135:8(771)

71. Tezduyar TE (2001) Finite element interface-tracking and interface-capturing techniques for flows with moving boundaries and interfaces. In: Proceedings of the ASME symposium on fluid-physics and heat transfer for macro- and micro-scale gas-liquid and

phase-change flows (CD-ROM), ASME Paper IMECE2001/HTD-24206, ASME, New York, New York

72. Stein K, Tezduyar TE, Benney R (2004) Automatic mesh update with the solid-extension mesh moving technique. Comput Methods Appl Mech Eng 193(21–22):2019–2032. https://doi.org/10.1016/j.cma.2003.12.046

73. Hsu MC, Akkerman I, Bazilevs Y (2011) High-performance computing of wind turbine aerodynamics using isogeometric analysis. Comput Fluids 49(1):93–100. https://doi.org/10.1016/j.compfluid.2011.05.002